

Experimental simulation of magma–carbonate interaction beneath Mt. Vesuvius, Italy

E. M. Jolis · C. Freda · V. R. Troll ·
F. M. Deegan · L. S. Blythe · C. L. McLeod ·
J. P. Davidson

Received: 18 July 2012 / Accepted: 16 July 2013 / Published online: 15 August 2013
© Springer-Verlag Berlin Heidelberg 2013

Abstract We simulated the process of magma–carbonate interaction beneath Mt. Vesuvius in short duration piston-cylinder experiments under controlled magmatic conditions (from 0 to 300 s at 0.5 GPa and 1,200 °C), using a Vesuvius shoshonite composition and upper crustal limestone and dolostone as starting materials. Backscattered electron images and chemical analysis (major and trace elements and Sr isotopes) of sequential experimental products allow us to identify the textural and chemical evolution of carbonated products during the assimilation process. We demonstrate that melt–carbonate interaction can be extremely fast (minutes), and results in dynamic

contamination of the host melt with respect to Ca, Mg and $^{87}\text{Sr}/^{86}\text{Sr}$, coupled with intense CO_2 vesiculation at the melt–carbonate interface. Binary mixing between carbonate and uncontaminated melt cannot explain the geochemical variations of the experimental charges in full and convection and diffusion likely also operated in the charges. Physical mixing and mingling driven by exsolving volatiles seems to be a key process to promote melt homogenisation. Our results reinforce hypotheses that magma–carbonate interaction is a relevant and ongoing process at Mt. Vesuvius and one that may operate not only on a geological, but on a human timescale.

Communicated by G. Moore.

Electronic supplementary material The online version of this article (doi:10.1007/s00410-013-0931-0) contains supplementary material, which is available to authorized users.

E. M. Jolis (✉) · V. R. Troll · F. M. Deegan · L. S. Blythe
Department of Earth Sciences, CEMPEG, Uppsala University,
Villavägen 16, 752 36 Uppsala, Sweden
e-mail: ester.jolis@geo.uu.se

C. Freda · V. R. Troll
Istituto Nazionale di Geofisica e Vulcanologia,
Via di Vigna Murata 605, 00143 Rome, Italy

F. M. Deegan
Department of Geosciences, Swedish Museum of Natural
History, 104 05 Stockholm, Sweden

C. L. McLeod · J. P. Davidson
Department of Earth Sciences, Durham University,
Science Labs, Durham DH1 3LE, UK

C. L. McLeod
Department of Earth and Atmospheric Sciences,
University of Houston, Houston, TX 77004, USA

Keywords Mt. Vesuvius · Magma–carbonate interaction · Crustal assimilation · CO_2 liberation · Experimental petrology

Introduction

The Mt. Somma-Vesuvius complex (1,281 m a. s. l.) comprises Mt. Somma, the >25–14 kyr strato-volcano, and Mt. Vesuvius, the recent cone which has grown within the older Mt. Somma caldera (e.g. Rolandi et al. 2004; Peccerillo 2005; Piochi et al. 2006; Di Renzo et al. 2007) and which we collectively term the “Vesuvius volcanic system” (VVS). The VVS is characterised by variable types of eruptions, ranging from effusive lava emission to explosive strombolian, sub-plinian and plinian events (Orsi et al. 1996; Peccerillo 2005; Paone 2006; Piochi et al. 2006). The VVS is sited on a sequence of Mesozoic and Cenozoic carbonates overlain by the Miocene siltstone sediments of the Campanian Plain (Brocchini et al. 2001; Civetta et al. 2004; Del Pezzo et al. 2006). Seismic tomography studies have suggested that the top of the Mesozoic carbonate

basement lies at around 2.5–3 km depth underneath the volcano (Zollo et al. 2002). The level at ~8–11 km depth has also been identified as a discontinuity, likely representing the top of the present day magma reservoir, which is probably linked to the base of the Mesozoic carbonate sequence at ~10–11 km depth (Zollo et al. 1996; Berrino et al. 1998; Auger et al. 2001). The VVS has been the focus of attention ever since the famous AD 79 eruption, being one of the most hazardous volcanic systems in Europe due to the densely populated Neapolitan region in its shadow. Although much is known concerning the volcano and its internal workings, a comprehensive understanding of the role of magma–crust interaction processes at the VVS has not yet been achieved.

The VVS produces slightly silica-undersaturated K-basalts and K-trachytes to highly silica-undersaturated K-tephrites and K-phonolites (D'Antonio et al. 1999; Paoone 2006; Piochi et al. 2006). The compositional variability of these magmas has been attributed to (1) mantle source variability (e.g. Ayuso et al. 1998; Peccerillo 1999; Somma et al. 2001), (2) differentiation and magma mixing (e.g. Turi and Taylor 1976; Civetta et al. 1991) and (3) contamination through carbonate assimilation (e.g. Rittmann 1933; Fulignati et al. 1995; Del Moro et al. 2001; Gilg et al. 2001). The role of carbonate assimilation has recently been documented for a significant number of volcanic systems emplaced in carbonate-rich crust, e.g. Popocatepetl, Colli Albani, and Merapi (e.g. Goff et al. 2001; Dallai et al. 2004; Schaaf et al. 2005; Chadwick et al. 2007; Freda et al. 2008). In fact, carbonate assimilation has been shown to occur over short timescales (minutes in experiments), and thus, the effect of carbonate decomposition in natural systems is thought to release significant amounts of CO₂ on timescales of hours to days (Deegan et al. 2010, 2011; Troll et al. 2012a). Such CO₂ influx into a volcanic system may not only have the potential to modify magma composition, but also the style of eruptive activity (Deegan et al. 2010, 2011; Dallai et al. 2011; Freda et al. 2011; Troll et al. 2012a, b). At the VVS, the presence of a thick carbonate basement, the frequent occurrence of skarn xenoliths, and the anomalous gas–chemical compositions unequivocally suggest that contamination through carbonate assimilation is a relevant process and may play an important role in the volcano's magma evolution and its eruptive behaviour and styles (cf. Freda et al. 1997; Del Moro et al. 2001; Gilg et al. 2001; Fulignati et al. 2004, 2005; Iacono-Marziano et al. 2009; Dallai et al. 2011). In this study, we report on a set of experiments designed to examine magma–carbonate interaction processes under controlled conditions (0.5 GPa and 1,200 °C), employing a composition representative of primitive VVS magmas and various local carbonates. Previously, magma–carbonate interaction experiments were run over hours to days to establish mineral–phase

relationships and the liquid line of descent in magmatic products affected by carbonates (e.g. Freda et al. 2008; Iacono-Marziano et al. 2008; Mollo et al. 2010). In contrast, our experimental series is designed to perform very short duration experiments (0, 60, 90 and 300 s; cf. Deegan et al. 2010), allowing the preservation of textures and phases developed during progressive carbonate breakdown and degassing. Coupled with in situ elemental and Sr-isotope constraints on our experiments, our data provide a more comprehensive understanding of the dynamics of magma–carbonate interaction in the VVS.

Experimental methods

The experiments were conducted in an end-loaded piston-cylinder apparatus at the HP-HT Laboratory of Experimental Volcanology and Geophysics of Istituto Nazionale di Geofisica e Vulcanologia (INGV, Rome, Italy). Experiments were carried out at 0.5 GPa equivalent to ca. ~13–14 km depth. This is the lowest pressure to which this end-loaded piston-cylinder apparatus is calibrated for, but is similar to the pressure inferred for the VVS magma reservoir (≥ 10 km depth; Zollo et al. 1996, 1998; Auger et al. 2001). The experimental temperature of 1,200 °C was calculated as the liquidus temperature of the starting composition at 0.5 GPa and initial water content of 2 wt %, using the MELTS algorithm (Ghiorso et al. 1994). The experimental temperature was reached in 6 min, which is sufficiently fast to preserve the textural relationships of the carbonate phase in the shortest duration experiments and allow inspection of the interaction between carbonate and the resulting melts in detail (see Deegan et al. 2010). Our experimental approach thus approximates the likely physical and chemical conditions of direct magma–carbonate interaction in the VVS.

The starting materials used in our experiments were a shoshonitic lava flow from the VVS (Di Renzo et al. 2007) and limestone and dolostone from the local Procida carbonate formation (e.g. Barberi et al. 1981; Civetta et al. 1991). The shoshonitic lava flow represents one of the least evolved rocks outcropping in the Neapolitan area. A shoshonite sample was first crushed, powdered, and doped with 2 wt % H₂O (added by microsyringe into an experimental capsule) and then melted at 1,250 °C and 0.5 GPa to produce a hydrated shoshonite glass. The hydrated glass was analysed for its major element composition (see Table 1) and was verified to be free of crystals and crystallites. Then, the hydrated shoshonite glass was powdered and used as the magmatic starting material in our experimental series.

The hydrated shoshonite powder was placed in platinum capsules (3.0 mm diameter, 12.0 mm long) together with

Table 1 Starting material composition

	Hydrous glass ^a	1 σ (9) ^b	Limestone CaVe1 Procida ^c	Dolostone CaVe3 Procida ^d
SiO ₂	49.85	0.21	0.02	0.02
TiO ₂	1.03	0.08	–	–
Al ₂ O ₃	15.95	0.67	–	–
FeO _t ^e	7.98	0.25	0.01	0.0
MnO	0.14	0.02	0.01	0.01
MgO	6.03	0.33	0.79	21.01
CaO	9.98	0.29	54.99	31.34
Na ₂ O	2.35	0.07	–	–
K ₂ O	4.01	0.19	–	–
P ₂ O ₅	0.70	0.09	0.02	0.0
CO ₂	–	–	44.11*	47.59*
H ₂ O	2	–	–	–
Total	100.02	–	100.00	100.00
Sr	735 [†]	–	299 ^{††}	89 ^{††}
⁸⁷ Sr/ ⁸⁶ Sr ^{†††}	0.706661 ± 8	–	0.7075 ± 1	0.7072 ± 1

^a Hydrous glass synthesised from natural powdered rock at $T = 1250$ °C and 0.5 GPa

^b 1 σ Standard deviation; the number in parenthesis represents the number of analyses

^c Lower Cretaceous limestone from Procida Formation

^d Triassic dolostone from Procida Formation

^{a,c,d} Major element composition of the starting materials were determined by electron microprobe at INGV and given in wt %

^e Total iron is given as FeO_t

* Fraction of CO₂ in the fluid phase was calculated assuming wt % CaCO₃ in the samples as equivalent to 100 wt % minus all other element oxides

[†] Strontium content for shoshonitic melt: Di Renzo et al. (2007)

^{††} Limestone and dolostone Sr contents were determined by ICP-emission spectrometry at AcmeLabs (Vancouver, Canada) and are given in ppm

^{†††} Strontium isotopes for: shoshonitic melt: Di Renzo et al. (2007); and for limestone and dolostone: Piochi et al. (2006) and Iannace et al. (2011)

fragments of ~6–8 mg (≤ 3.0 mm side length) of either limestone or dolostone (Table 1). The capsules were then welded shut and positioned in tandem into a 19.1 mm NaCl-crushable alumina–Pyrex assembly. This means that the two capsules were placed side by side in the same assembly, one containing the hydrated shoshonite glass and limestone and the other the hydrated shoshonite glass and dolostone. The tandem approach has the advantage that it allows a direct comparison between limestone- and dolostone-bearing experiments as physical parameters (pressure, temperature and time) are otherwise identical. The capsules were surrounded by pyrophyllite powder to prevent water loss (see Freda et al. 2001). Further details of the experimental approach can be found in Freda et al. (2008) and Deegan et al. (2010).

Analytical methods

The experimental products were analysed using a JEOL-JXA8200 electron microprobe (EMPA) and a JEOL-6500F

field emission-scanning electron microscope (FE-SEM) at INGV Rome. Microprobe analyses were performed using an accelerating voltage of 15 kV, a beam current of 5 nA and a beam diameter of 5 μ m for glass and 1 μ m for mineral analyses (see, e.g. Iezzi et al. 2008, for analytical details). Sodium and potassium were analysed first to reduce possible volatilisation effects. The average standard deviation (1 σ) of major element oxides (in wt %) is 0.34 for SiO₂, 0.06 for TiO₂, 0.11 for Al₂O₃, 0.10 for FeO, 0.03 for MnO, 0.07 for MgO, 0.16 for CaO, 0.05 for Na₂O, 0.03 for K₂O, 0.04 for P₂O₅.

Microsampling of the experimental products for their Sr-isotope ratios was performed at the Arthur Holmes Isotope Laboratory, Department of Earth Sciences, Durham University, UK, using a New Wave MicromillTM and following the technique outlined in Charlier et al. (2006). The Micromill consists of a binocular microscope, a mill, a stage, which controls movement reproducible to ± 1 μ m and a computer workstation which integrates all the components (Charlier et al. 2006). Sampling sites were selected using BSE images to precisely locate the drill points and

avoid fractures and bubbles. The samples were milled along selected areas to a depth of 30 μm . Milling was carried out under a single drop of Milli-Q water to collect the drilled sample dust. The sample and Milli-Q water mixture was pipetted off and transferred directly to a “gold boat” for processing through micro-Sr column chemistry as described in Charlier et al. (2006). After processing, the samples were analysed by TIMS using a Thermo-Finnigan Triton system (see Font et al. 2008). During the analysis period (July to August 2010), the international Sr standard NBS-987 was analysed with sample sizes ranging from 3 to 600 ng. The overall average Sr isotopic ratios for the NBS-987 measurements during this period ($n = 26$) was 0.710261 ± 0.000016 , within error of the published $^{87}\text{Sr}/^{86}\text{Sr}$ value of 0.710248 ± 0.000023 (2σ) ($n = 427$) reported by Thirlwall (1991). Aliquots of the dissolved milled samples were analysed for their trace element concentrations by inductively coupled plasma mass spectrometry (ICP-MS) using a Thermo Electron Element II system at Durham University, UK. Procedural details are provided in Font et al. (2008). Total procedural blanks ($n = 5$) were less than 22 pg for all elements analysed. Sr blanks averaged 0 ± 1 pg (2σ , $n = 5$).

Results

Features of the experimental products

The experimental conditions for all ten experiments are given in Table 2, and representative electron-microprobe analytical traverses of two experimental products are reported in Table 3.

Three major phases were identified: (1) two distinct glasses (representing melts), Ca-normal and either Ca- or Ca–Mg-rich, which are identified in BSE images as dark and bright in colour, respectively. A contamination front

(CF) usually separates the two glass domains (Fig. 1). (2) Crystalline phases, such as calcite, pyroxene and olivine (Figs. 2, 3), and (3) a vapour phase represented by bubbles (e.g. Fig. 1). In the following section, the main features of the experimental products are described to explain the dynamics of magma–crust interaction in the experiments and to report on the differences between limestone- and dolostone-bearing experiments.

Limestone-bearing experiments

In the limestone-bearing experimental products, for $t_d = 0$ –90 s, two distinct glass regions were observed (Fig. 1a–c): (1) a Ca-normal glass domain, very similar in composition to the shoshonite starting material (av. 49.85 wt % SiO_2 , 9.98 wt % CaO) and (2) a Ca-rich glass domain with an interface between the two (CF). Within the CF region, the Ca-normal glass domain shows progressive depletion in silica and enrichment in CaO, grading into the Ca-rich melt domain (Fig. 4), with aluminium strongly mimicking the behaviour of silica. The interfacial regions (CF) hence involve progressive physico-chemical mixing between the two dominant glass domains and an interfacial boundary between the Ca-rich and Ca-normal domains is observed in all experiments. The solid phases are dendritic microcrystals of calcite (Fig. 2) produced in Ca-rich areas of the Ca-rich glass domains. These crystals represent quench crystals formed from local enrichment of previous calcite components in the experimental melts. Notably, the $t_d = 300$ s run is characterised by a more homogeneous Ca-rich glass, vapour (bubbles) and no crystals (Fig. 1d).

Dolostone-bearing experiments

The dolostone-bearing experimental products contain either glass and vapour phases ($t_d = 0$ s; Fig. 1e) or crystals, glass, and vapour phases ($t_d = 60$ –300 s; Fig. 1f–h).

Table 2 Experimental conditions

Run #	Experimental time t_d (s)	Pressure (GPa) ^a	Temperature (°C) ^a	Limestone (mg)	Dolostone (mg)	Hydrous glass ~2 wt % H_2O (mg)
PC443-V5	0	0.5	1,200	6.1	–	29.6
PC448-V9	60	0.5	1,200	8.2	–	33.3
PC442-V3	60	0.5	1,200	6.3	–	28.8
PC441-V1	90	0.5	1,200	6.8	–	24.2
PC-445 V7	300	0.5	1,200	7.2	–	26.0
PC443-V6	0	0.5	1,200	–	6.0	30.0
PC448-V10	60	0.5	1,200	–	7.7	34.2
PC442-V4	60	0.5	1,200	–	7.0	29.6
PC441-V2	90	0.5	1,200	–	6.0	30.0
PC445-V8	300	0.5	1,200	–	7.1	26.4

^a Pressure and temperature uncertainties are ± 0.02 GPa and ± 5 °C, respectively

Table 3 Representative electron-microprobe chemical analyses

	Traverse 1																	
	Ca-normal glass			Contamination front (CF)			Ca-rich glass			Contamination front (CF)			Ca-normal glass					
<i>Experimental run # PC443-V5 limestone-bearing</i>																		
SiO ₂	50.3	49.7	49.8	49.2	42.2	32.3	29.8	30.4	35.3	41.0	39.2	39.3	42.6	48.5	49.7	49.3	50.1	
TiO ₂	1.0	1.0	1.0	1.0	0.7	0.7	0.7	0.7	0.7	0.8	0.8	0.9	0.9	1.0	1.0	1.0	0.9	
Al ₂ O ₃	15.6	15.5	15.3	15.2	13.2	9.6	9.1	9.7	11.3	12.8	12.2	12.5	13.3	15.2	15.3	15.9	16.2	
FeO	6.6	6.5	6.1	5.6	4.8	4.5	4.8	4.9	4.7	5.7	6.1	6.1	6.4	5.9	7.2	7.0	7.1	
MnO	0.1	0.1	0.2	0.1	0.1	0.1	0.1	0.1	0.1	0.1	0.1	0.1	0.1	0.1	0.1	0.1	0.1	
MgO	5.5	5.5	5.3	4.9	4.3	4.4	3.8	3.5	4.1	5.0	5.4	5.2	5.3	4.8	5.7	5.6	5.7	
CaO	9.1	9.3	10.2	11.7	22.2	30.9	31.5	30.2	29.3	21.6	23.8	23.7	20.9	13.0	9.6	9.1	9.1	
Na ₂ O	3.0	2.9	2.9	2.6	1.7	1.3	1.1	0.9	1.1	1.5	1.3	1.4	1.5	2.2	2.6	2.5	2.6	
K ₂ O	5.3	5.4	5.8	5.7	3.1	1.8	1.5	1.4	2.1	3.1	2.4	2.2	2.3	4.2	4.4	4.4	4.2	
P ₂ O ₅	0.6	0.7	0.6	0.6	0.4	0.5	0.5	0.4	0.3	0.6	0.5	0.4	0.5	0.7	0.6	0.6	0.6	
SrO	0.1	0.2	0.1	0.1	0.0	0.0	0.1	0.1	0.0	0.0	0.1	0.1	0.1	0.1	0.1	0.1	0.0	
BaO	0.1	0.1	0.2	0.1	0.0	0.0	0.1	0.0	0.1	0.1	0.2	0.1	0.1	0.3	0.2	0.1	0.1	
Total ^a	97.3	96.9	97.5	96.8	92.7	86.1	83.0	82.5	89.1	92.4	92.1	92.0	93.9	95.7	96.5	95.8	96.8	
											Traverse 2							
											Contamination front (CF)							
											Ca–Mg-normal glass							
											Ca–Mg-rich glass							
<i>Experimental run # PC442-V4 dolostone-bearing</i>																		
SiO ₂	48.9	48.8	49.0	48.7	48.6	44.1	40.9	41.6	38.5	37.0	45.1	47.9	46.5	43.9	47.0	46.6		
Al ₂ O ₃	1.1	0.9	0.9	1.0	0.9	1.0	1.1	0.7	0.8	0.7	1.0	1.0	0.9	1.0	1.0	0.9		
TiO ₂	16.7	16.6	16.6	16.3	16.4	14.7	13.8	14.0	12.7	12.1	15.4	16.4	15.8	15.8	16.2	16.3		
FeO	6.5	6.3	6.6	6.2	6.1	6.6	6.9	6.1	5.7	5.4	5.7	5.3	5.5	5.7	5.5	5.5		
MnO	0.1	0.1	0.1	0.1	0.1	0.1	0.2	0.1	0.1	0.1	0.1	0.1	0.1	0.1	0.1	0.1		
MgO	5.8	5.7	5.7	5.8	5.8	7.8	8.7	8.4	9.2	9.0	7.1	5.5	7.2	7.8	6.6	6.7		
CaO	9.1	9.2	9.1	9.4	10.2	14.4	16.6	17.1	19.9	20.8	13.4	10.1	12.6	14.9	10.5	11.2		
Na ₂ O	3.0	2.9	3.1	3.1	2.9	2.2	1.9	1.9	1.6	2.4	2.4	2.9	2.6	2.3	3.0	3.0		
K ₂ O	3.9	4.0	4.0	4.2	4.1	2.6	2.2	2.6	2.1	2.3	3.7	4.9	3.6	3.0	4.3	4.2		
P ₂ O ₅	0.6	0.5	0.6	0.6	0.7	0.6	0.6	0.6	0.6	0.5	0.5	0.7	0.5	0.6	0.6	0.6		
BaO	0.1	0.1	0.1	0.1	0.1	0.1	0.1	0.1	0.0	0.1	0.0	0.1	0.0	0.2	0.1	0.1		
SrO	0.2	0.1	0.2	0.0	0.1	0.1	0.2	0.2	0.0	0.1	0.3	0.3	0.2	0.1	0.1	0.1		
Total ^a	96.1	95.3	96.0	95.4	95.9	94.2	93.1	93.4	91.3	90.4	94.8	95.2	95.7	95.5	95.0	95.5		

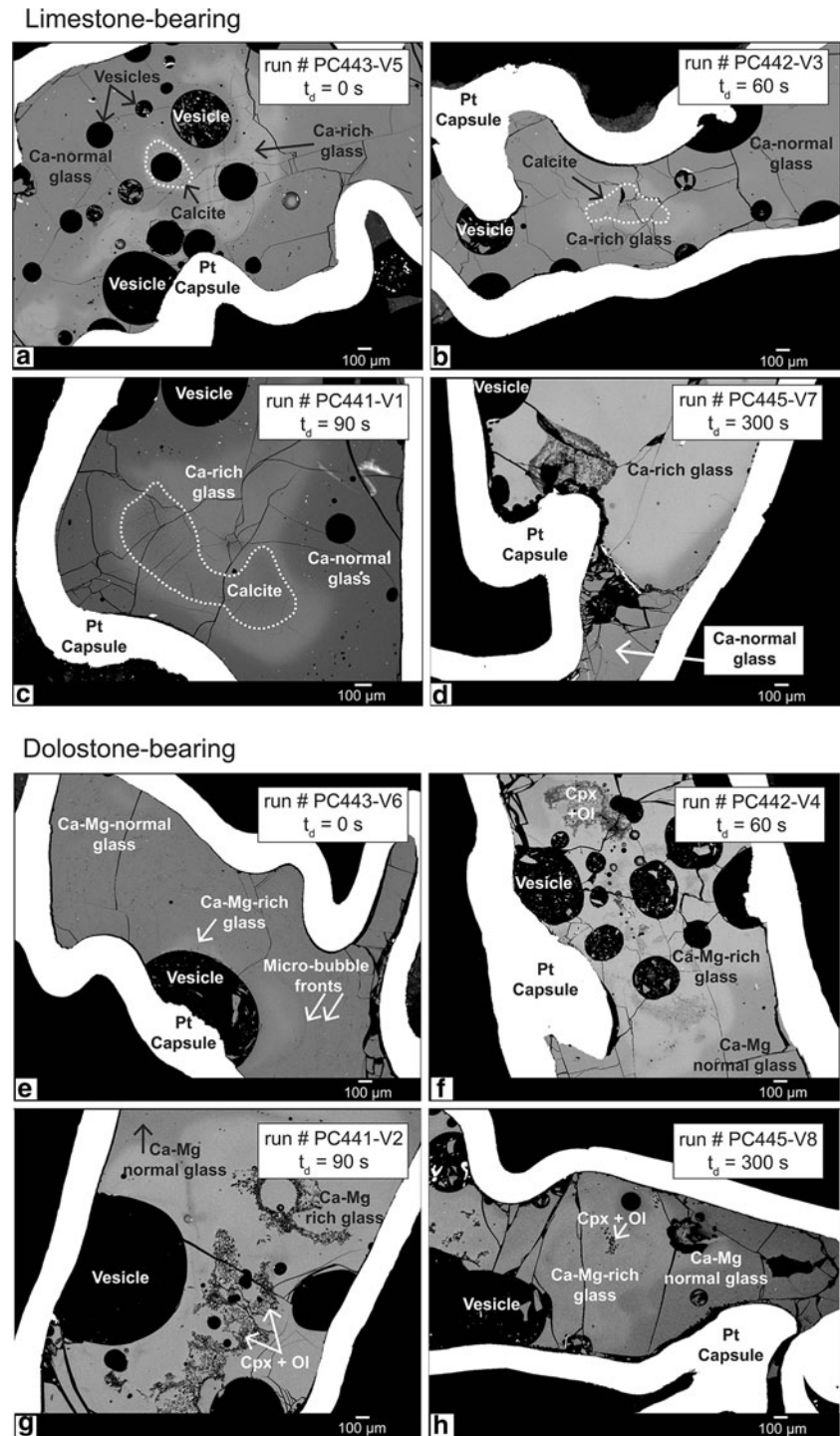
Analyses shown are from the experimental glass regions: Ca-normal, Ca-rich and contamination front (CF)

^a The low totals obtained are due to one of the following reasons: (a) microbubbles (cf. Deegan et al. 2010), (b) increased CO₂ solubility in alkaline and ultrapotassic melts in general (cf. Behrens et al. 2009) or (c) increased CO₂ solubility in our Ca-rich experimental melt (Moore 2008)

The results of chemical traverses through the various glass regions are shown in Fig. 5. The dolostone-bearing experiments show a normal glass with chemical composition similar to the starting material, a contaminated glass (Ca–Mg enriched), and CF regions in between the two. In the CF areas, it is possible to distinguish a progressive dilution of silica and coeval calcium and magnesium enrichment relative to the shoshonite starting material (Fig. 5). Crystalline phases in the dolostone-bearing experiments are olivine and pyroxene. Analyses of all mineral phases are provided in the Online Resource 1

(Table OR1). The ternary diagram in Fig. 3 shows the crystalline phases in the Ca₂SiO₄–Mg₂SiO₄–Fe₂SiO₄ and in the CaSiO₃–MgSiO₃–FeSiO₃ systems. Pyroxene is dominant over olivine and is highly enriched in CaO (>20 wt %) and MgO (10–14.4 wt %), in agreement with its occurrence in the interfacial area, i.e. depletion in SiO₂ and enrichment in CaO, MgO and Al₂O₃ (Fig. 3a). The olivine compositions are close to forsterite (Fo_{95–96.7}), but with a notable enrichment in CaO (1.31–2.36 wt %; Fig. 3b) and thin likely more Fe-rich outer rims. The olivine crystals (~10–20 μm size) are euhedral, and the pyroxene display

Fig. 1 BSE images of experimental products with increasing experimental durations ($t_d = 0\text{--}300$ s): limestone-bearing experiments (a–d) and dolostone-bearing experiments in (e–h). Experiments show (1) a solid phase, i.e. calcite crystallite domains—marked with a broken white line in images a–c—and olivine and pyroxene crystals in images f–h; (2) a melt phase, i.e. Ca-normal, and Ca-rich and Ca–Mg-rich glasses; and (3) a vapour phase, preserved as bubbles. Note the contrasting brightness between Ca-rich and Ca–Mg-rich, and Ca-normal glasses in the images (light and dark colour, respectively)



ehedral to subhedral shapes, which points to direct growth of olivine and pyroxene from contaminated melts (Fig. 3).

Vapour phase in experimental products

The vapour phase in our experiments is preserved as numerous vesicles (bubbles) that formed at the

contamination front predominantly from exsolved CO_2 (see below). Vesicles were observed in all experimental runs in different quantities, sizes and spatial distributions. For dolostone-bearing experiments, the vesicles' spatial distribution is not random; rather, the bubbles tend to concentrate close to contaminated areas. In contrast, for limestone-bearing experiments, the bubbles have a tendency to nucleate in the Ca-rich melt domains and migrate

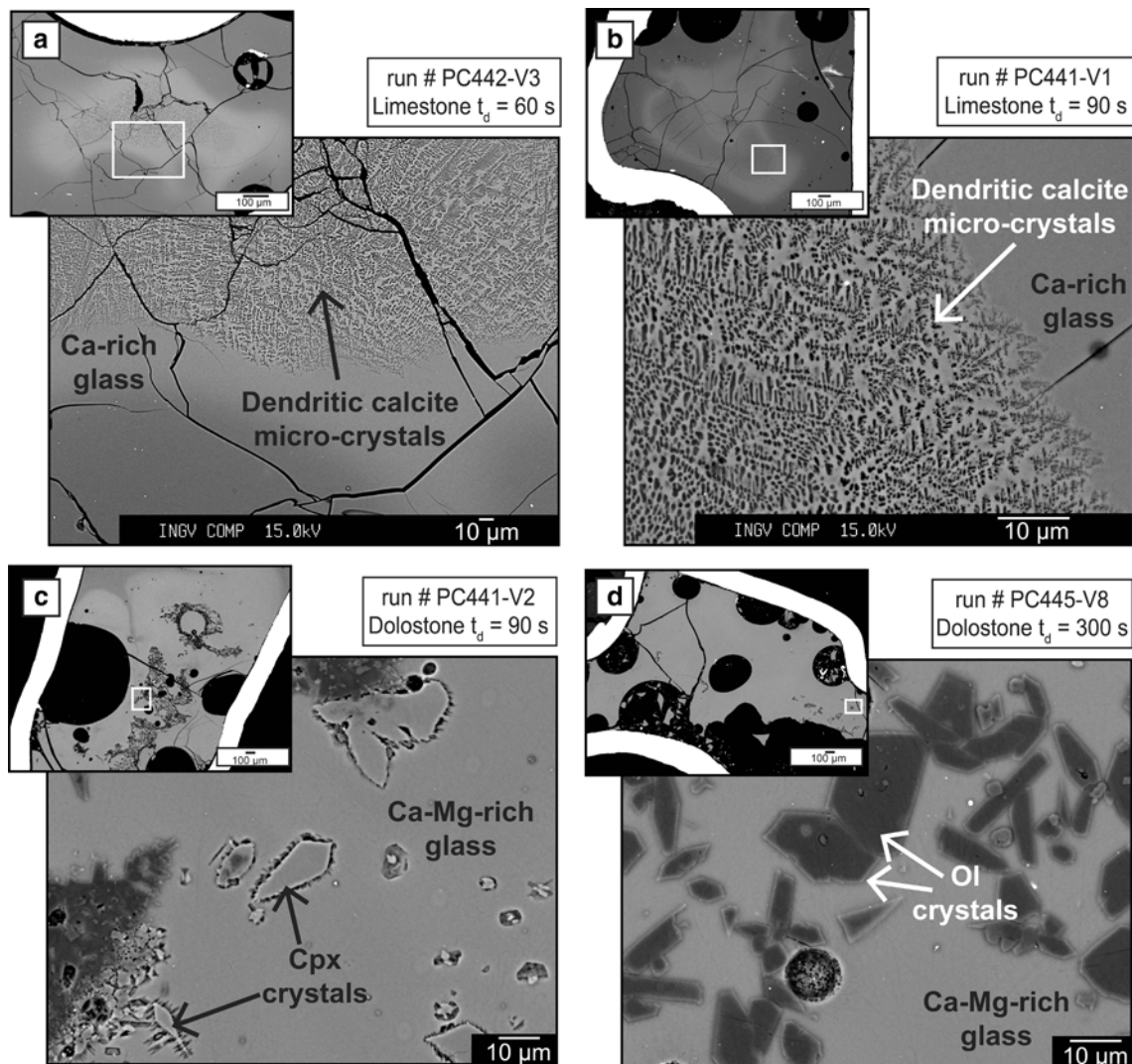


Fig. 2 BSE images showing dendritic micro-crystals of calcite in limestone-bearing experiments at $t_d = 60$ and 90 s (**a**, **b**) and clinopyroxene and olivine crystals from the dolostone-bearing experiments at $t_d = 90$ and 300 s (**c**, **d**). *Ol* olivine and *Cpx* clinopyroxene

into the Ca-normal glass as reflected by different generations of vesicles and micro-bubble fronts (Fig. 1). Bubble sizes increase from a micrometre to a millimetre scale with progressive experimental run-time (Blythe et al. 2012), reflecting initial bubble nucleation that is followed by progressive bubble growth and coalescence.

Strontium isotope compositions in the experimental products

The Sr-isotope variations in limestone- and dolostone-bearing experiments are illustrated in Figs. 6 and 7, and the data are reported in Table 4. All trace element concentrations in the drilled samples can be found in the Online Resource 2 (Table OR2). The micro-Sr-isotope analyses

show significant $^{87}\text{Sr}/^{86}\text{Sr}$ variability in each experiment (0.706729 ± 10 – 0.707023 ± 33 in limestone-bearing and 0.707017 ± 8 – 0.707743 ± 10 in dolostone-bearing experiments). The analysed Ca-normal glass has low $^{87}\text{Sr}/^{86}\text{Sr}$ values (0.706729 ± 10 – 0.706896 ± 40) similar to those of the shoshonite starting material (0.706661 ± 8 ; Di Renzo et al. 2007). In contrast, the more radiogenic $^{87}\text{Sr}/^{86}\text{Sr}$ values (0.706951 ± 17 – 0.707743 ± 10) correspond to Ca- or Ca-Mg-rich domains, with $^{87}\text{Sr}/^{86}\text{Sr}$ ratios that trend towards those of the carbonates of the Campanian region (0.7072 ± 1 – 0.7093 ± 8 ; Civetta et al. 1991; Piochi et al. 2006; Iannace et al. 2011). Three of the microdrilled experiments were analysed in the CF, showing $^{87}\text{Sr}/^{86}\text{Sr}$ signatures that fall in between the respective Ca- or Ca-Mg-rich and Ca-normal glass compositions of these experiments (Figs. 6, 7).

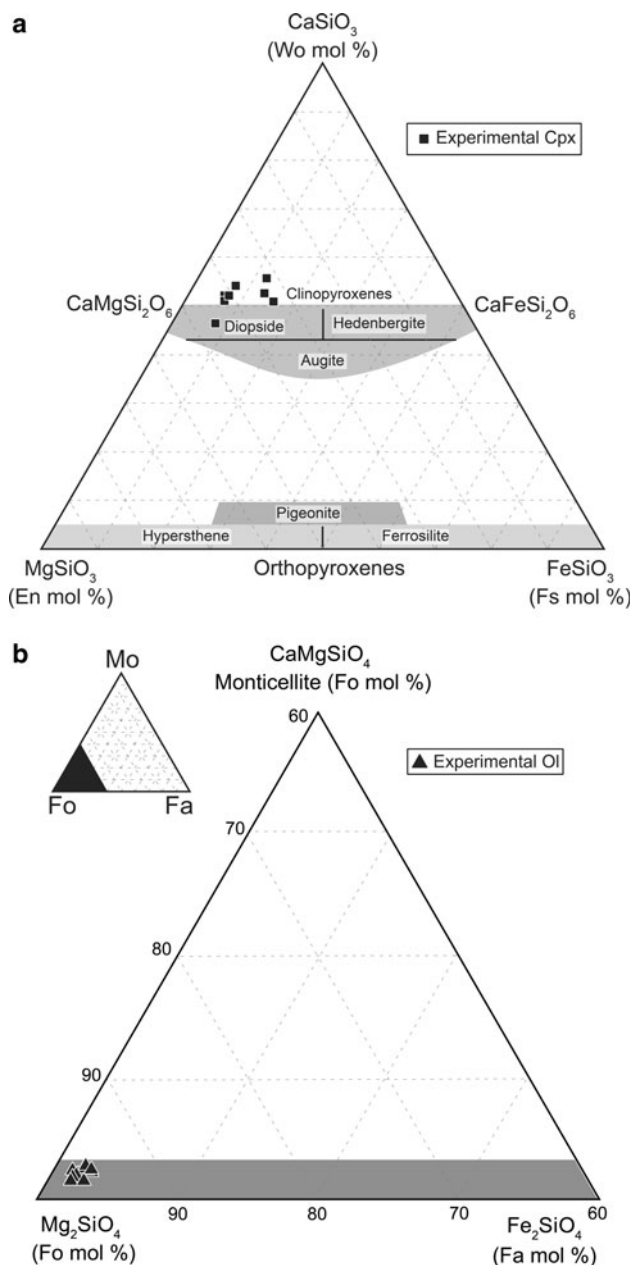


Fig. 3 Ternary diagrams of mineral compositions in dolostone-bearing experiments. Composition of pyroxenes in the CaSiO_3 – MgSiO_3 – FeSiO_3 system (a). Composition of olivines in the Ca_2SiO_4 – Mg_2SiO_4 – Fe_2SiO_4 system (small inset triangle). The bottom left hand corner of the small triangle is shown in large (b)

Discussion

Effects of magma–carbonate interaction

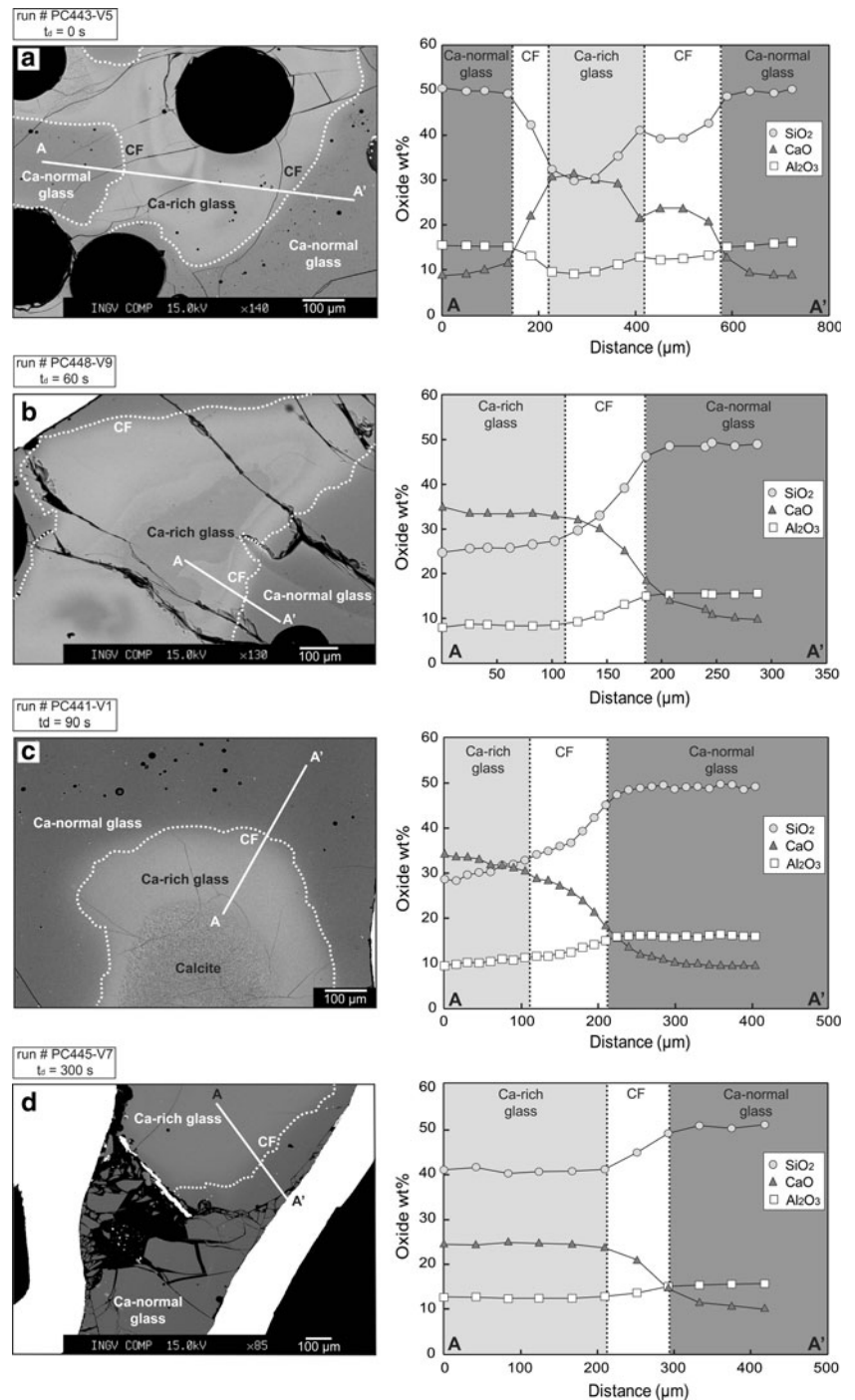
Magma–carbonate interaction and consequent carbonate assimilation allows for several possible reaction routes, ranging from direct dissolution to formation of a series of intermediate products, such as the various skarn assemblages frequently observed (e.g. Gaeta et al. 2009; Mollo

et al. 2010; Troll et al. 2012b). The net result of this interaction is an overall release of CaO by limestone and CaO and MgO by dolostone into the host magmas(s), and associated liberation of CO_2 (cf. Mollo et al. 2012; Troll et al. 2012a). The experiments simulate direct magma–carbonate interaction, which is demonstrated by the chemical profiles and by the abundant occurrence of bubbles in the experimental products. A recent experimental investigation using a basaltic–andesite composition from Merapi volcano and Indonesian carbonate as starting material, and employing analogous pressure (0.5 GPa), temperature (1,200 °C) and water content (~ 2 wt %), showed similar processes of magma–carbonate interaction at work (Deegan et al. 2010). These authors established that carbonate break-down began during the experimental heating phase (approximately 6 min.), and the time required to complete carbonate assimilation was probably no more than ca. 330 s at their target experimental conditions. In contrast to the Merapi experiments, we observe that no original carbonate is preserved in any of our experimental products (Figs. 1, 2), implying that carbonate dissociation and complete dissolution occurred before the target temperature of 1,200 °C was reached. The highest degree of physico-chemical mixing between melt domains occurs between $t_d = 60$ and 90 s (i.e. mixing initially increases with time; Figs. 8, 9). At $t_d \sim 300$ s, contaminated melt dominates almost the entire volume of the experimental charge, leaving normal melts at the rims only, i.e. mixing is approaching completion. It should be noted though that calcite (or alternatively pyroxene and olivine) crystallised where local enrichment of certain elements was the result of magma–carbonate interaction and implies that chemical homogenisation between melts is limited within the timeframe of our experiments, i.e. the run-time for the experiments does not permit complete homogenisation. The Vesuvius experiments, in contrast to the Merapi ones, therefore display a significantly shorter timescale of magma–carbonate interaction, suggesting faster reaction rates between the shoshonite melt and the carbonate (limestone and dolostone) under otherwise similar pressure and temperature conditions.

The chemical variations between glass domains in limestone- and dolostone-bearing experiments can be approximated by binary mixing models with the starting materials (limestone, dolostone and shoshonite) as end-members. Based on these models, we provide an estimate of the maximum degree of mixing between melts in each experimental step. The degree of mixing varies mainly with the experimental duration (t_d) (Figs. 8, 9) and maximum mixing degrees are often confined to spatially limited zones of about 100–200 μm in experiments up to 90 s (Figs. 4, 5).

The limestone-bearing experiments reflect this variation on the maximum degree of mixing between carbonate and

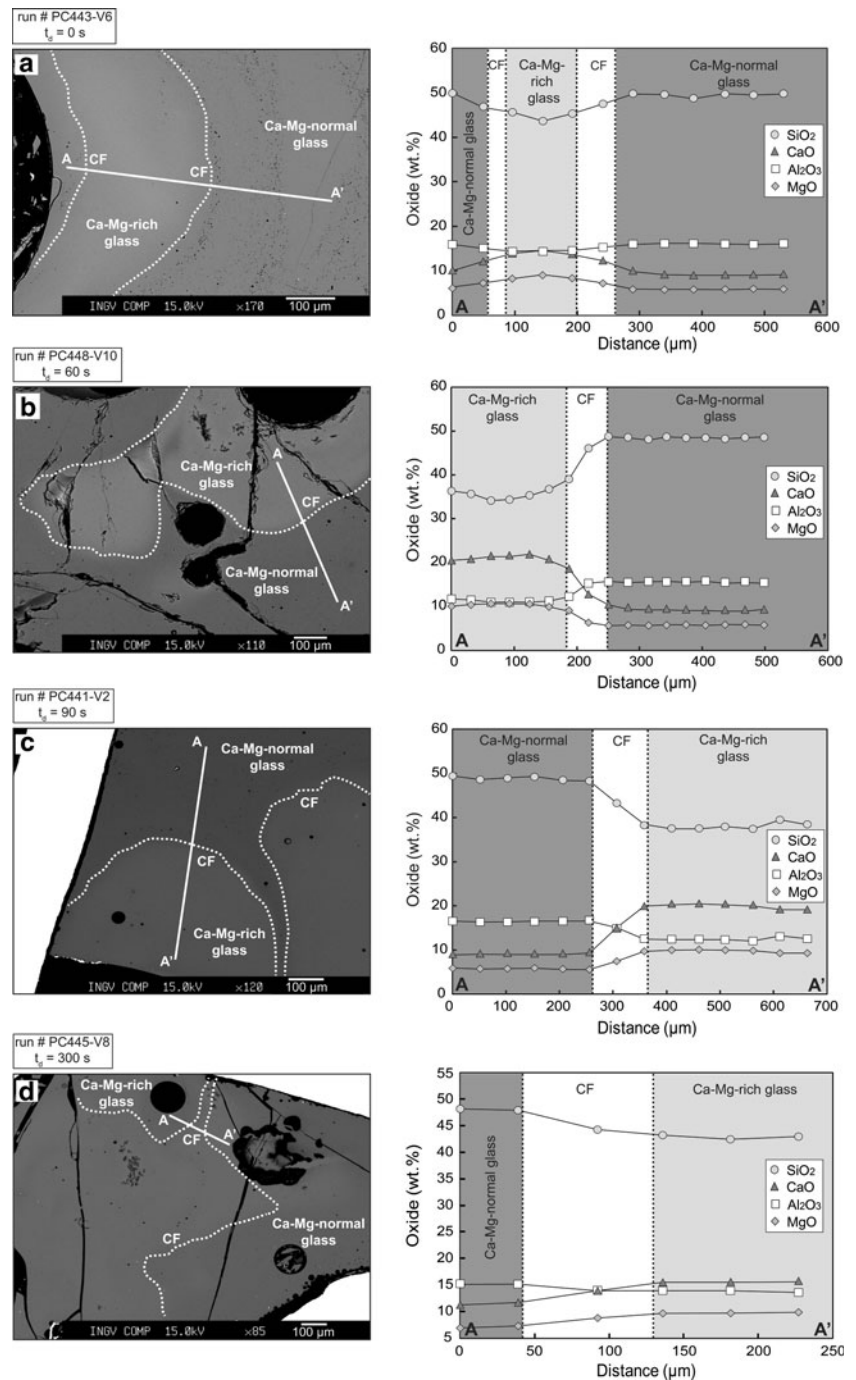
Fig. 4 Representative microprobe chemical traverses in 0, 60, 90 and 300 s limestone-bearing experiments (a–d). The white lines in the images show the EMPA traverses (A to A') that correspond to the plots on the right. The Ca-normal and Ca-rich glasses are dark and pale grey in colour, respectively, and are separated by a dashed white line. The contamination front (CF) is the interfacial region between Ca-normal and Ca-rich domains. This area corresponds to a physico-chemical mixing and diffusion interface between the glass domains. Note that the width of the CF (delimited by vertical dashed lines on the right graphs) differs in the various experimental runs



shoshonite through time (Fig. 8; see Online Resource 3 Fig OR1) and similar degrees of mixing are observed for elements such as MgO, Al₂O₃ or NaO₂. The maximum degree of limestone component in the melt phase (limestone: shoshonite, weight ratio) is (1) ~40:60 at $t_d = 0$ s, (2) ~50:50 at $t_d = 60$ s, and (3) ~60:40 at $t_d = 90$ s. At (4) $t_d = 300$ s, the resultant melt is almost homogenous, representing a mixture between dissolved carbonate and shoshonite melt of about 25:75. For the dolostone-bearing experiments, the maximum degree of dolostone component

in the melt phase (dolostone: shoshonite, weight ratio) for experimental duration is (Fig. 9; see Online Resource 3 Fig OR2): (1) ~15:85 at $t_d = 0$ s, (2) ~45:55 at $t_d = 60$ s, (3) ~45:55 at $t_d = 90$ s, and (4) about 25:75 at the longest experimental duration of 300 s. These models demonstrate that the degree of mixing is time-dependent and generally greater for the longer duration experiments. For the experiments between 0 and 90 s, the resultant melts are inhomogeneous and in disequilibrium since the system undergoes various degrees of diffusive and convective

Fig. 5 Representative microprobe chemical traverses in 0, 60, 90 and 300 s dolostone-bearing experiments (a–d). The *solid white lines* drawn on the images show the EMPA traverses (A to A') corresponding to the plots on the *right*. The contact between contaminated and uncontaminated melts is highlighted with *white dashed lines* (CF). See also Fig 4



mixing in addition to crystal growth and resorption (e.g. calcite, pyroxene and olivine). In contrast, at $t_d = 300$ s, in both limestone- and dolostone-bearing experiments, a hybrid melt containing about 25 wt % CaO begins to form as the result of pervasive mixing and progressive homogenisation (Figs. 8, 9; Online Resource 3). Pure binary mixing between two melt end-members should follow a linear relationship for a regular element pair (e.g. CaO vs. SiO₂), which, however, is not always observed in our experiments (Figs. 8, 9). The observed variations may reflect different

mobilities of trace and major elements over very short timescales during incipient mingling and mixing, producing complex and fluctuating patterns that deviate from straight mixing trends. This deviation is most pronounced in the dolostone-bearing experiments. There, the mixing trajectory appears to move furthest from the straight mixing trend, probably as a result of crystal growth (olivine and pyroxene) and associated Mg removal from the melt that shifts the Ca/Mg ratio of the melt away from that of an ideal mixture (cf. De Campos et al. 2008; Perugini et al. 2006,

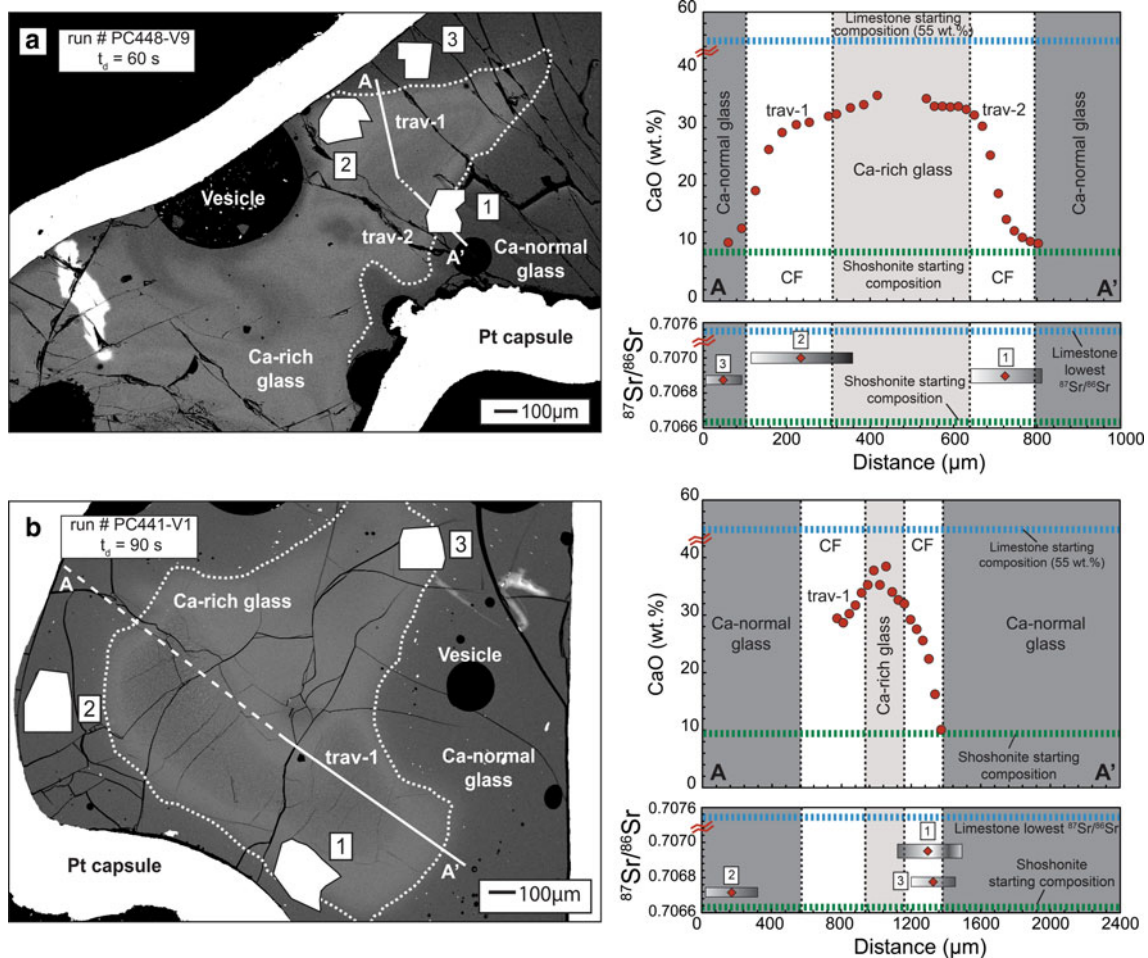


Fig. 6 $^{87}\text{Sr}/^{86}\text{Sr}$ and CaO wt % profiles in the 60 s (a) and the 90 s (b) limestone-bearing experiments. The *solid lines* in the BSE images show different traverses in a single experiment (from A to A'). Drilled areas are *numbered* and highlighted in *white* on the BSE images. The *right side of images for a and b* correspond to the CaO wt % from EMPA traverse (*upper diagram*) and the $^{87}\text{Sr}/^{86}\text{Sr}$ -isotope ratios of the drilled areas (*lower diagram*). The height of the *rectangles* in the

$^{87}\text{Sr}/^{86}\text{Sr}$ diagram represents the ± 2 SE analytical uncertainty and their locations relative to the EMPA traverse data are approximate (see Table 4). The *dark- and pale-shaded areas* represent the glass domains observed in our experiments and the *blue and green horizontal-dashed lines* are the CaO wt % and $^{87}\text{Sr}/^{86}\text{Sr}$ ratios of the starting materials

2008). We also estimated “apparent diffusivities” of SiO_2 , Al_2O_3 , MgO and CaO across the contamination front in the limestone-bearing experiments (see Online Resource 4). The results yield apparent diffusivities in m^2/s of $8.5 \cdot 10^{-10}$ – $8.6 \cdot 10^{-7}$ for SiO_2 , $8.5 \cdot 10^{-10}$ – $1.9 \cdot 10^{-9}$ for Al_2O_3 , $8.5 \cdot 10^{-10}$ – $1.1 \cdot 10^{-8}$ for MgO and $3.4 \cdot 10^{-11}$ – $6.3 \cdot 10^{-6}$ for CaO in the 60 and 300 s experiments, respectively (Online Resource 4). The determined values are between two and five orders of magnitude greater than well-established diffusivities for these elements (e.g. Watson 1982; Watson and Jurewicz 1984; Baker 1991; Leshner et al. 1996; Liang et al. 1996; Zhang 1993, 2010) and, moreover, they vary between the different duration experiments. These data imply that although diffusion is a relevant process at play, the overall elemental gradients observed must be the result of a combination of processes including mingling, mixing,

convection, and local crystal growth (Figs. 1, 8, 9). These additional processes can all affect the melt interface and thus overprint diffusion profiles in the experimental charges. In our experiments, the process of physical mixing and mingling observed between the melt domains is driven by volatiles that exsolve during carbonate assimilation (Fig. 1), which likely contributes most strongly to melt homogenisation on the timescale of our experiments. Crystal growth, on the other hand, is influenced by carbonate break-down in our experiments. Limestone, for example, contributes to local calcite-saturation whereas dolostone provides additional CaO and MgO thereby promoting crystallisation of Ca-rich pyroxene and Ca–Mg-rich olivine (cf. Metz and Milke 2012). The crystallisation of these mineral phases in our experiments is a function of the state of the contaminated melt, i.e. it is dependent on melt

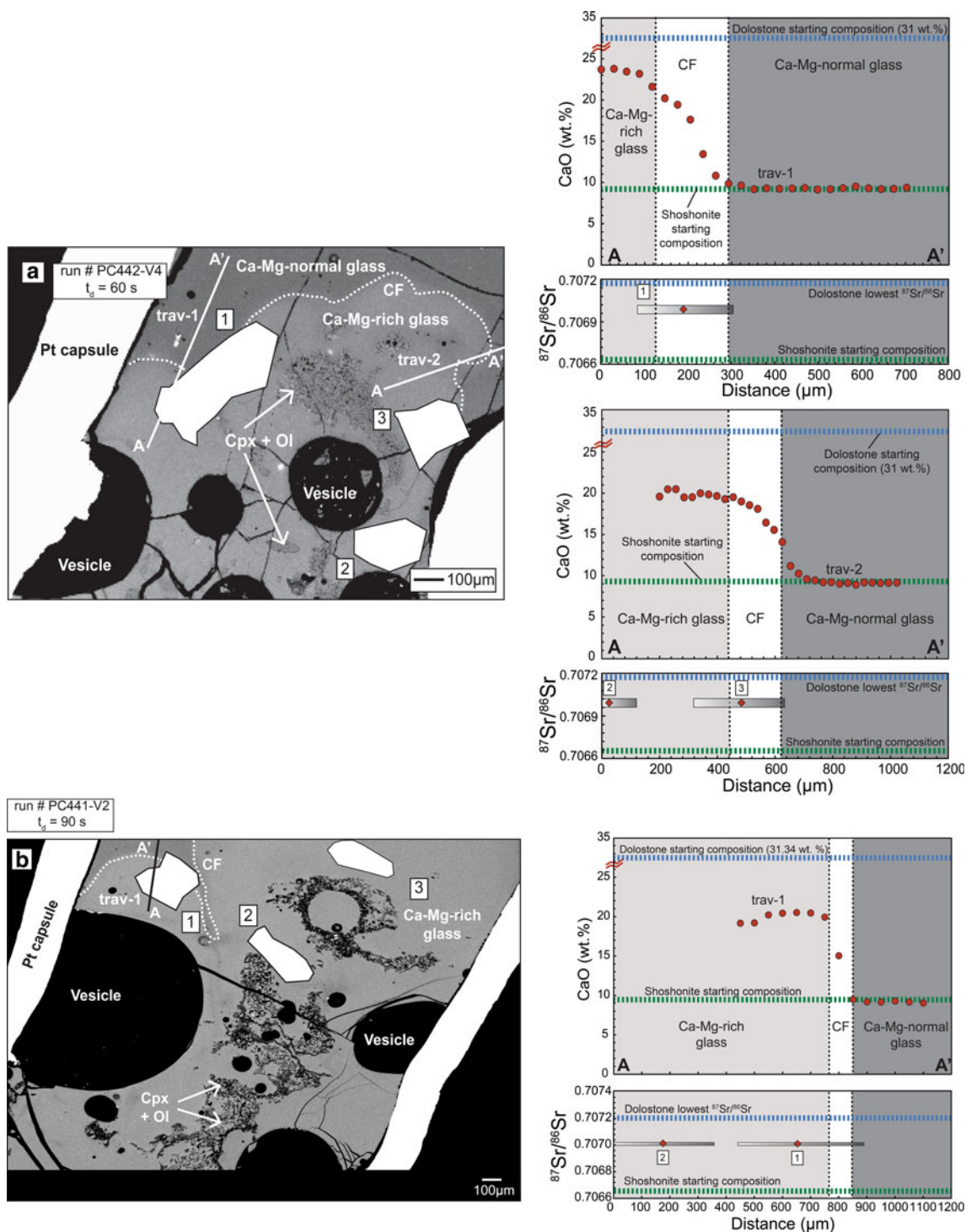


Fig. 7 $^{87}\text{Sr}/^{86}\text{Sr}$ and CaO wt % profiles in the dolostone-bearing experiments. **a** BSE image of the 60 s experiment and **b–d** show the 90 s experiment. The white/black lines in the images show different traverses in a single experiment (A to A'). The diagrams on the right side illustrate CaO wt % (upper diagram) and $^{87}\text{Sr}/^{86}\text{Sr}$ (lower

diagram) for the different traverses and drill holes, respectively. The height of the rectangles in the $^{87}\text{Sr}/^{86}\text{Sr}$ diagram includes the ± 2 SE analytical uncertainty and their locations of the drill holes relative to the EMPA traverses are approximate. The traverse in **b** extends beyond the BSE image. Abbreviations as in Fig 6

domains that are locally enriched in CaO and MgO prior to full homogenisation. Notably, the growth of high-Mg olivine from dolostone contaminated melt raises the

possibility that high-Fo olivine is not always an indicator for primitive or primary magma compositions in volcanic systems and particularly not in the VVS.

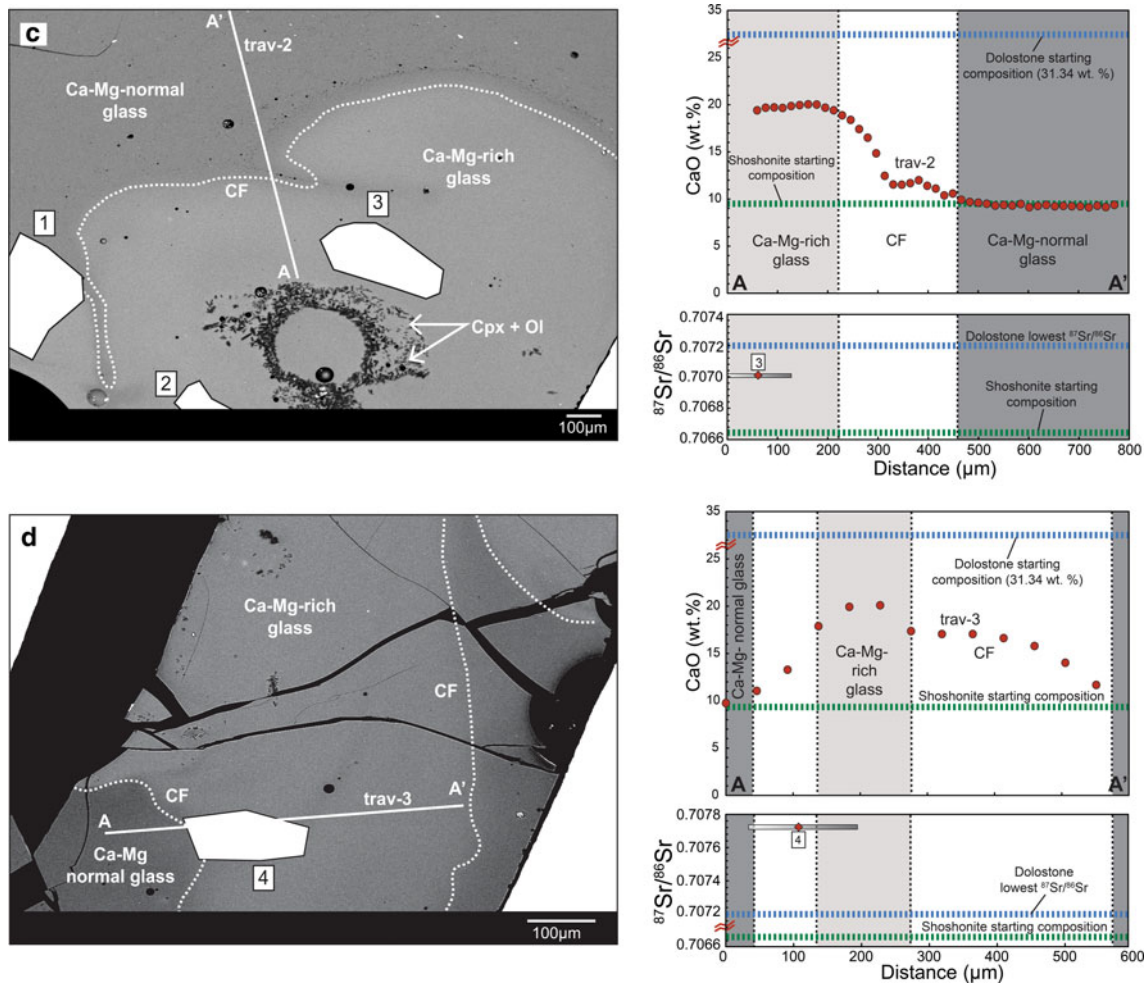


Fig. 7 continued

 $^{87}\text{Sr}/^{86}\text{Sr}$ composition of the experimental products

The $^{87}\text{Sr}/^{86}\text{Sr}$ -isotope variations provide a first order approximation of the degree of carbonate assimilation in our experiments. The Sr-isotope ratios and Sr concentration for Mt. Vesuvius shoshonitic magmas range between 0.7067 and 0.7071 and from 735 to 1,093 ppm, respectively (Di Renzo et al. 2007). The $^{87}\text{Sr}/^{86}\text{Sr}$ -isotope ratios and Sr concentration of carbonate-rich lithologies from the Campanian region were previously thought to range between 0.7075 and 0.7090 and from 500 to 1,000 ppm, respectively (Civetta et al. 1991; Piochi et al. 2006; Del Moro et al. 2001). More recent studies on the same carbonates now also report lower values of $^{87}\text{Sr}/^{86}\text{Sr}$ to be present, e.g. 0.7072–0.7074 (Iannace et al. 2011) with associated Sr concentrations of as little as 41–151 ppm, implying that these carbonates are highly heterogeneous in their Sr concentrations and $^{87}\text{Sr}/^{86}\text{Sr}$ composition (see below).

The Sr-isotope profiles of the experimental products display a broad correlation of higher $^{87}\text{Sr}/^{86}\text{Sr}$ ratios with

increasing CaO wt %, i.e. with the most contaminated drill samples, whereas the non-contaminated glasses show Sr-isotope ratios that overlap with those of the natural shoshonite starting material (Fig. 10a). The $^{87}\text{Sr}/^{86}\text{Sr}$ ratios observed in the CF regions usually fall in between these extremes and frequently form mixtures with intermediate $^{87}\text{Sr}/^{86}\text{Sr}$ signatures (Figs. 6, 7). Indeed, in this respect, the isotopic variations observed within each individual experiment can be explained as the result of mixing between “normal” and “contaminated” melts. The situation appears somewhat more complex, however, when using binary mixing trajectories between the published values for the shoshonite and for the various carbonate $^{87}\text{Sr}/^{86}\text{Sr}$ values as well as for a high (500–1,000 ppm) and a low (<500 ppm) Sr concentration group that are now available in the literature (e.g. Civetta et al. 1991; Piochi et al. 2006; Del Moro et al. 2001; Di Renzo et al. 2007; Iannace et al. 2011). For the VVS shoshonite, a $^{87}\text{Sr}/^{86}\text{Sr}$ ratio of 0.7067 and a Sr concentration of 735 ppm was chosen (Table 1). For the carbonates, five values were selected (C_1 – C_5) because their Sr-isotope ratios

Table 4 Strontium concentration and isotope ratios in micro-milled experimental glasses

Sample, location	Sr (ppm)	$^{87}\text{Sr}/^{86}\text{Sr}$	± 2 SE
<i>PC448-V9 (60 s)</i>			
L-V9.1	423	0.706896	0.000040
L-V9.2	482	0.707023	0.000033
L-V9.3	606	0.706864	0.000030
<i>PC441-V1 (90 s)</i>			
L-V1.1	396	0.706951	0.000017
L-V1.2	596	0.706729	0.000010
L-V1.3	228	0.706795	0.000009
<i>PC442-V4 (60 s)</i>			
D-V4.1	478	0.707022	0.000012
D-V4.2	534	0.707022	0.000017
D-V4.3	578	0.707023	0.000007
<i>PC441-V2 (90 s)</i>			
D-V2.1	547	0.707021	0.000014
D-V2.2	563	0.707021	0.000012
D-V2.3	548	0.707017	0.000008
D-V2.4	602	0.707743	0.000010

L limestone and D dolostone; 1, 2, 3 and 4 are the sampled areas in each experiment, which correspond to the drilled areas labelled in Figs. 6 and 7

SE standard error

are so variable that a single composition cannot represent the available data range on limestone and dolostone from the Campanian region. For example, the high Sr concentration

carbonate (500–1,000 ppm) cannot explain the range of Sr isotopic values measured in the experiments as only one drill sample, the most radiogenic one (D-V2.4, 0.707743), falls into the shoshonite— C_1 — C_2 —mixing space (Fig. 10b). The best fit for the remaining drill data is achieved using low-Sr (<500 ppm) carbonates (C_2 – C_5). Employing these possible end-member(s), all remaining experimental data fall into the theoretically possible mixing space. This observed range of $^{87}\text{Sr}/^{86}\text{Sr}$ in the experimental Ca-rich melts implies on the one hand that the contaminant used in our experiments is highly inhomogeneous on a mm to sub-mm-scale, which is consistent with the realisation that the Campanian carbonates are heterogeneous regarding their Sr-isotope values as well as their Sr concentrations (e.g. Iacono-Marziano et al. 2008; Iannace et al. 2011). On the other hand, most carbonate material in our experiments appears to have lower Sr concentrations than the shoshonite melt (see Table 1; Di Renzo et al. 2007). A contaminated shoshonite may therefore be less radiogenic than previous predictions of contamination have suggested on the basis of the high $^{87}\text{Sr}/^{86}\text{Sr}$ and Sr concentration values available for the Procida formation at that time (e.g. Ayuso et al. 1998; Iacono-Marziano et al. 2008). Considering the full range of possible mathematical solutions, including the recent low-Sr and low- $^{87}\text{Sr}/^{86}\text{Sr}$ end-members (Iannace et al. 2011; Table 1), the most intensely contaminated experimental drill samples then calculate to mixtures of between 55 and 75 % carbonate-derived $^{87}\text{Sr}/^{86}\text{Sr}$ relative to unmodified shoshonite (Fig. 10b).

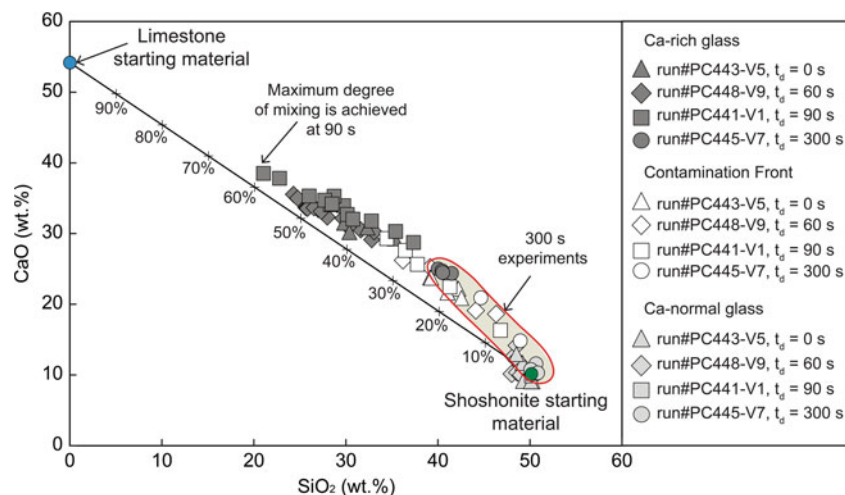


Fig. 8 Compositional summary diagram of all limestone-bearing experiments. Binary mixing trajectory between shoshonite and limestone is illustrated. The experiments are represented by: triangles for $t_d = 0$ s ($n = 17$); diamonds for $t_d = 60$ s ($n = 27$); squares for $t_d = 90$ s ($n = 21$); circles for $t_d = 300$ s ($n = 11$). The glass domains and the interface region are given as: dark grey = Ca-rich, pale grey = Ca-normal, and white = contamination front. The maximum degree of chemical mixing of ambient melt with carbonate-

derived CaO is reached at $t_d = 90$ s and equates to about 60 %. Note that at $t_d = 300$ s (highlighted with a red line), the system has progressively homogenised (less than 25 % carbonate-derived CaO in the mixture). The small displacement of CaO and SiO_2 above the linear binary mixing trajectory reflects fluctuations of these elements as a consequence of transport through convection and interdiffusion between the experimental melts (see text for details and Online Resource 3 Fig 1)

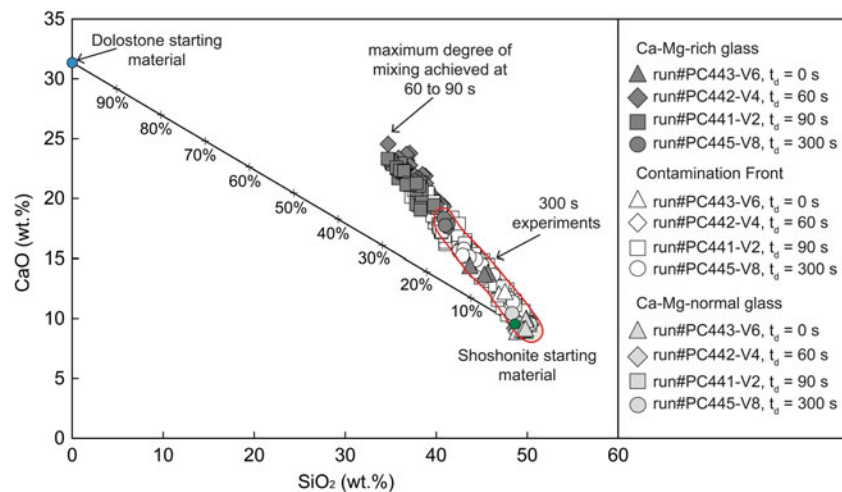


Fig. 9 Compositional summary diagram of all dolostone-bearing experiments. Binary mixing trajectory between shoshonite and dolostone is represented. The symbols for each experiment and the colours of glass domains are the same as in Fig. 8. The total number of data points in each experiment is: $n = 12$ for $t_d = 0$ s; $n = 80$ for $t_d = 60$ s; $n = 137$ for $t_d = 90$ s; $n = 23$ for $t_d = 300$ s. For these experiments, the system reached its maximum degree of mixing at

$t_d = 60$ to 90 s. For $t_d = 300$ s (highlighted with a red line), the glass has again adopted a more homogenous composition. The deviations from the binary mixing trajectory are likely a coupled consequence of melt transport, as in the limestone-bearing experiments, but was affected by simultaneous olivine and pyroxene growth and associated Mg removal from the melt (see also Online Resource 3 Fig 2)

The noteworthy aspect of these results is that relatively primitive compositions at the VVS (e.g. shoshonite) may represent contaminated magma even in the absence of particularly high Sr-isotope ratios or high Sr elemental concentrations, as large amounts of contamination by a low $^{87}\text{Sr}/^{86}\text{Sr}$ and low-Sr ppm carbonate will only exhibit a small effect on the Sr-isotope composition of the magma. A CaO and Sr relationship, as previously predicted for substantial limestone assimilation, cannot be expected if low Sr-isotope contaminants and variable Ca and Mg ratios in limestones versus dolostones (and their resulting calc-silicate skarns) are considered to influence the system in addition to pure limestone uptake. The lack of a clear CaO–Sr relationship is hence no longer an argument against carbonate assimilation (cf. Ayuso et al. 1998). Coupled with the occurrence of high-Mg olivine and pyroxene in our dolostone-bearing experimental products, a mineral association known from some primitive VVS samples (e.g. Dallai et al. 2011), low-Sr dolostone may in fact be a key contaminant for the VVS.

CO₂ liberation during magma–carbonate interaction

Dissolved volatiles in silicate melts play an important role in defining physical properties of magmas, e.g. density, viscosity, and vesicularity, and thus influence ascent behaviour and eruptive styles (e.g. Dingwell 1996; Baker et al. 2005; Deegan et al. 2010; Lesne et al. 2010). The most abundant volatiles in magmas are H₂O and CO₂, which are commonly dissolved in different percentages

depending on melt composition, pressure, temperature, and degree of saturation (e.g. Zhang and Stolper 1991). In particular, solubility experiments on shoshonite under conditions similar to those used in this study, i.e. 1,250 °C and 0.4 GPa, show that water solubility is about 8 wt %, while CO₂ solubility is limited to <3,000 ppm. Under CO₂ saturated conditions (>3,000 ppm), only 2 wt % H₂O is soluble, however (Di Matteo et al. 2006; Vetere et al. 2011). This is broadly consistent with H₂O and CO₂ solubilities predicted for shoshonite by the numerical model of Papale et al. (2006), which yields solubilities of 1.9 wt % and 3,449 ppm for H₂O and CO₂, respectively, at the pressure and temperature conditions of our experiments. In our experiments, therefore, H₂O and CO₂ coexist in the melt. During carbonate break-down and assimilation, the progressive increase in CaO and CO₂ in the melt will affect both the CO₂ and H₂O solubilities (see Table 3; Holloway 1976; Watson et al. 1982; Blank and Brooker 1994; Holloway and Blank 1994; Dixon 1997; Botcharnikov et al. 2005; Moore 2008) and will provide CO₂ to the melt until volatile saturation is achieved. At this point, a fluid phase will form that will likely contain only a small portion of H₂O since the solubility of water in our experimental system is close to our starting content of 2 wt % according to the models of Papale et al. (2006) and Vetere et al. (2011). Either model implies that although some H₂O is transferred from the melt to the fluid phase on CO₂ saturation, most of the water remains in the melt. Carbonate assimilation will then progressively add more CO₂ to the fluid phase, meaning that in our experimental charges, the

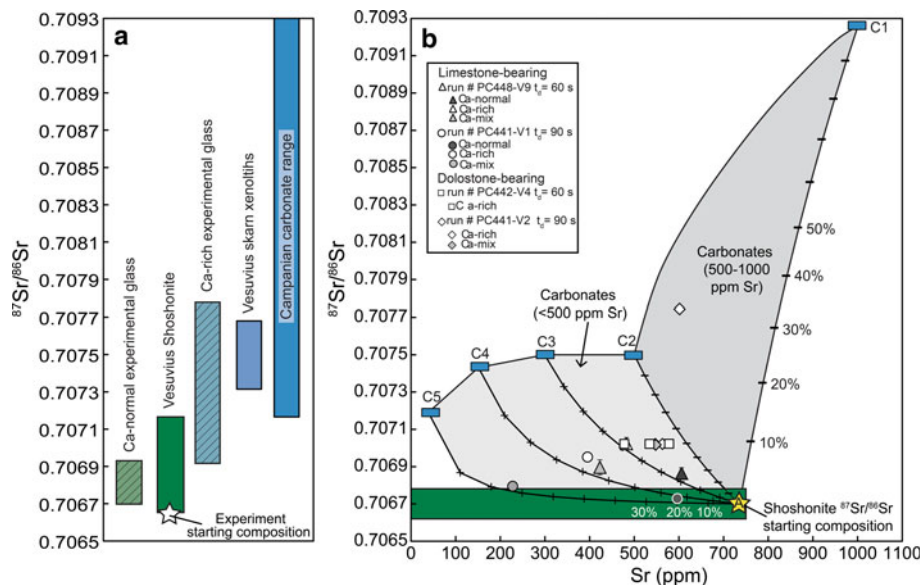


Fig. 10 **a** $^{87}\text{Sr}/^{86}\text{Sr}$ values for our experimental glasses in comparison with VVS shoshonite magma compositions, Vesuvius skarn xenoliths, and local carbonate crust. The Ca-normal glass is within the range of the natural shoshonite magmas, whereas the contaminated glass is displaced towards crustal values and overlaps with the range of skarns reported from the VVS. **b** $^{87}\text{Sr}/^{86}\text{Sr}$ vs. Sr (ppm) diagram illustrates possible binary mixing relationships. Triangles and circles represent the limestone-bearing experiments for t_d at 60 and 90 s, respectively, whereas squares and diamonds are the dolostone-bearing experimental products for the same experimental durations. The mixing trajectories A–C₁ and A–C₂ define a mixing space between the

shoshonite end-member (A) and the high $^{87}\text{Sr}/^{86}\text{Sr}$ and high Sr concentrations reported from some parts of the nearby carbonate crust. The mixing trajectories A–C₂, A–C₃, A–C₄ and A–C₅ form the mixing space between shoshonite (A) and the low $^{87}\text{Sr}/^{86}\text{Sr}$ and low-Sr ppm carbonates reported from the Campanian region (see text for details). The majority of the drilled experimental glass compositions fall within the low-Sr carbonate-mixing space (mixing curves A–C₂ to A–C₅), implying mixtures of between 55 and 75 % carbonate-derived $^{87}\text{Sr}/^{86}\text{Sr}$ relative to shoshonite. Literature data from: Civetta et al. (1991), Di Renzo et al. (2007), Del Moro et al. (2001), Piochi et al. (2006), Iannace et al. (2011)

final mixed H₂O–CO₂ vapour phase is strongly CO₂ dominated.

The potential amount of CO₂ released by carbonate assimilation in the experimental charges can be assessed using an average amount of carbonate and shoshonitic melt of 6.9 and 28.38 mg, respectively. The complete breakdown of carbonate during our experiments will liberate 3.05 mg of CO₂, which corresponds to 4.98 wt % of CO₂ in the experimental charge as a whole (vs. ≤ 2 wt % H₂O). Therefore, the experimental approach presented here shows that CO₂ liberation during carbonate assimilation can be significant under crustal magma reservoir conditions and may be an important factor in promoting explosive behaviour at the VVS.

Implications of the Vesuvius volcanic system

Magma–carbonate interaction is a relevant process in the VVS and is characterised by (1) the abundance of high temperature skarn xenoliths in the erupted products (e.g. Fulignati et al. 1998, 2004, 2005; Del Moro et al. 2001), (2) crustally derived CO₂ detected via the chemical and isotope composition of Vesuvius fumaroles (e.g. Iacono-Marziano et al. 2009), and (3) the $\delta^{18}\text{O}$ isotope

composition of mafic VVS minerals that interacted with sedimentary carbonate already at considerable depths (Dallai et al. 2011). Judging from our experiments, interaction between carbonate and Vesuvius shoshonite is indeed a viable and likely very fast process (minutes to hours). Moreover, we have shown how this process will progressively enrich the host melt in CaO and likely also MgO (from dolostone), while generating a CO₂-rich fluid phase. The experimental products show that CO₂ is generated directly at the melt–carbonate interface. In nature, this gas phase would form bubbles at crustal levels (Holloway and Blank 1994) and be transported upwards through the magma plumbing and conduit system. Therefore, CO₂ fluxes at the VVS are probably highly variable over different timescales, and CO₂ emissions measured in volcanic fumaroles at Vesuvius, that show a dominance of crustal over mantle-derived CO₂ (e.g. Iacono-Marziano et al. 2009), may be explained by the process modelled in our experiments. Conceivably, large quantities of CO₂ may be rapidly liberated during, e.g. renewed magma injection into shallow levels of the VVS reservoir system, where magma–carbonate interaction and carbonate assimilation have the potential to promote erratic explosive behaviour over short timescales (cf. Deegan et al. 2010, 2011; Freda et al. 2011). This implication would appear to be relevant

to other volcanic systems as well, notably Merapi, Indonesia (Chadwick et al. 2007; Deegan et al. 2010), the Colli Albani, Italy (Freda et al. 2011), Popocatepetl, Mexico (Goff et al. 2001; Schaaf et al. 2005), and maybe even Yellowstone, USA (Werner and Brantley 2003), that like Vesuvius are emplaced within some type of carbonate crust. We conclude that magma–carbonate interaction in the upper crust is likely a significant process operating beneath Vesuvius, but is variable in intensity. This interaction likely involves limestone and dolostone compositions and is not always easily quantified by conventional petrochemical indices (e.g. Sr–Ca relationships). Independently of the exact nature of the carbonate considered, our experiments demonstrate that magma–carbonate interaction can rapidly release considerable quantities of crustal CO₂ with potentially direct consequences on explosive versus effusive eruptive behaviour of the volcanic system.

Acknowledgments We are grateful to L. Civetta for providing the starting materials. V. Misiti and A. Cavallo kindly helped during the experimental and EMPA work at INGV and G. Nowell kindly supported the micro-drilling and strontium isotope analysis at Durham University. Discussion with S. Mollo, G. Orsi, C. Siebe, L. Dallai, and T. Walter is much appreciated. We thank D. Baker and two anonymous referees for constructive reviews. We also thank the Swedish Science Foundation (VR), the Centre for Natural Disaster Science (CNDS), Uppsala University (UU), the Royal Swedish Academy of Science (KVA), the Irish Research Council for Science (IRCSET), and the Istituto Nazionale di Geofisica e Vulcanologia (INGV) for generous financial support of our work.

References

- Auger E, Gasparini P, Virieux J, Zollo A (2001) Seismic evidence of an extended magmatic sill under Mt. Vesuvius. *Science* 294:1510–1512
- Ayuso RA, De Vivo B, Rolandi G, Seal RR II, Paone A (1998) Geochemical and isotopic (Nd–Pb–Sr–O) variations bearing on the genesis of volcanic rocks from Vesuvius, Italy. *J Volcanol Geotherm Res* 82:53–78
- Baker DR (1991) Interdiffusion of hydrous dacitic and rhyolitic melts and the efficacy of rhyolite contamination of dacitic enclaves. *Contrib Mineral Petrol* 106:462–473
- Baker DR, Freda C, Brooker RA, Scarlato P (2005) Volatile diffusion in silicate melts and its effects on melt inclusions. *Ann Geophys* 28:699–717
- Barberi F, Bizouard H, Clocchiatti R, Metrich N, Santacroce R, Sbrana A (1981) The Somma-Vesuvius magma chamber: a petrological and vulcanological approach. *Bull Volcanol* 44:295–315
- Behrens H, Misiti V, Freda C, Vetere F, Botcharnikov RE, Scarlato P (2009) Solubility of H₂O and CO₂ in ultrapotassic melts at 1200 and 1250°C and pressure from 50 to 500 MPa. *Am Mineral* 94:105–120
- Berrino G, Corrado G, Riccardi U (1998) Sea gravity on the Gulf of Naples: a contribution to delineating the structural pattern of the Vesuvian area. *J Volcanol Geotherm Res* 82:139–150
- Blank JG, Brooker RA (1994) Experimental studies of carbon dioxide in silicate melts: solubility, speciation, and stable carbon isotope behaviour. In: Carroll MR, Holloway JR (ed) *Volatiles in magmas*. *Rev Mineral* 20:157–186
- Blythe L, Misiti V, Masotta M, Taddeucci J, Freda C, Troll VR, Deegan FM, Jolis EM (2012) Viscosity controlled magma–carbonate interaction: a comparison of Mt. Vesuvius (Italy) and Mt. Merapi (Indonesia). *Geophys Res Abstracts* 14, EGU2012-4779-1
- Botcharnikov R, Freise M, Holtz F, Behrens H (2005) Solubility of C–O–H mixtures in natural melts: new experimental data and implication range of recent models. *Ann Geophys* 48:633–646
- Brocchini D, Principe C, Castradori D, Laurenzi MA, Gorla L (2001) Quaternary evolution of the southern sector of the Campanian Plain and early Somma-Vesuvius activity: insights from the Trecase 1 well. *Mineral Petrol* 73:67–91
- Chadwick JP, Troll VR, Ginibre C, Morgan D, Gertisser R, Waight TE, Davidson JP (2007) Carbonate assimilation at Merapi volcano, Java, Indonesia: insights from crystal isotope stratigraphy. *J Petrol* 48:1793–1812
- Charlier BLA, Ginibre C, Morgan D, Nowell GM, Pearson DG, Davidson JP, Ottley CJ (2006) Methods for microsampling and high-precision analysis of strontium and rubidium at single crystal scale for petrological and geochronological applications. *Chem Geol* 232:114–133
- Civetta L, Galati R, Santacroce R (1991) Magma mixing and convective compositional layering within the Vesuvius magma chamber. *Bull Volcanol* 53:287–300
- Civetta L, D’Antonio M, De Lorenzo S, Di Renzo V, Gasparini P (2004) Thermal and geochemical constraints on the ‘deep’ magmatic structure of Mt. Vesuvius. *J Volcanol Geotherm Res* 133:1–12
- D’Antonio M, Civetta L, Orsi G, Pappalardo L, Piochi M, Carandente A, De Vita S, Di Vito MA, Isaia R, Southon J (1999) The present state of the magmatic system of the Campi Flegrei caldera based on the reconstruction of its behaviour in the past 12 ka. *J Volcanol Geotherm Res* 91:247–268
- Dallai L, Freda C, Gaeta M (2004) Oxygen isotope geochemistry of pyroclastic clinopyroxene monitors carbonate contributions to Roman-type ultrapotassic magmas. *Contrib Mineral Petrol* 148:247–263
- Dallai L, Cioni R, Boschi C, D’Orsiano C (2011) Carbonate-derived CO₂ purging magma at depth: influence on the eruptive activity of Somma-Vesuvius, Italy. *Earth Planet Sci Lett* 310:84–95
- De Campos CP, Dingwell DB, Perugini D, Civetta L, Fehr TK (2008) Heterogeneities in Magma Chambers: insights from the behavior of major and minor elements during mixing experiments with natural alkaline melts. *Chem Geol* 256:130–144
- Deegan FM, Troll VR, Freda C, Misiti V, Chadwick JP, McLeod CL, Davidson JP (2010) Magma–carbonate interaction processes and associated CO₂ release at Merapi volcano, Indonesia: insights from experimental petrology. *J Petrol* 51:1027–1051
- Deegan FM, Troll VR, Freda C, Misiti V, Chadwick JP (2011) Fast and furious: crustal CO₂ release at Merapi volcano, Indonesia. *Geol Today* 27:57–58
- Del Moro A, Fulignati P, Marianelli P, Sbrana A (2001) Magma contamination by direct wall rock interaction: constraints from xenoliths from the wall of carbonate-hosted magma chamber (Vesuvius 1944 eruption). *J Volc Geotherm Res* 112:15–24
- Del Pezzo E, Bianco F, De Siena L, Zollo A (2006) Small scale shallow attenuation structure at Mt. Vesuvius, Italy. *Phys Earth Planet Inter* 157:257–268
- Di Matteo V, Mangiacapra A, Dingwell DB, Orsi G (2006) Water solubility and speciation in shoshonitic and latitic composition from Campi Flegrei Caldera (Italy). *Chem Geol* 229:113–124

- Di Renzo V, Di Vito MA, Arienzo I, Carandente A, Civetta L, D'Antonio M, Giordano F, Orsi G, Tonarini S (2007) Magmatic History of Somma-Vesuvius on the basis of new geochemical and isotopic data from a deep borehole (Camaldoli della Torre). *J Petrol* 48:753–784
- Dingwell DB (1996) Volcanic dilemma: flow or blow? *Science* 273:1054–1055
- Dixon JE (1997) Degassing of alkali basalts. *Am Mineral* 82:368–378
- Font L, Davidson JP, Pearson DG, Nowell GM, Jerram DA, Ottley CJ (2008) Sr and Pb isotope micro-analysis of plagioclase crystals from Skye lavas: an insight into open-system processes in a flood basalt province. *J Petrol* 49:1449–1471
- Freda C, Gaeta M, Palladino DM, Trigila R (1997) The Villa Senni Eruption (Alban Hills, central Italy): the role of H₂O and CO₂ on the magma chamber evolution and on the eruptive scenario. *J Volcanol Geotherm Res* 78:103–120
- Freda C, Baker D, Ottolini L (2001) Reduction of water loss from gold-palladium capsules during piston cylinder experiments by use of pyrophyllite powder. *Am Mineral* 86:234–237
- Freda C, Gaeta M, Misiti V, Mollo S, Dolfi D, Scarlato P (2008) Magma-carbonate interaction: an experimental study on ultrapotassic rocks from Alban Hills (Central Italy). *Lithos* 101:397–415
- Freda C, Gaeta M, Giaccio B, Marra F, Palladino DM, Scarlato P, Sottili G (2011) CO₂-driven large mafic explosive eruptions: the Pozzolane Rosse case study from the Colli Albani Volcanic District (Italy). *Bull Volcanol* 73:241–256
- Fulignati P, Gioncada A, Sbrana A (1995) The magma chamber related hydrothermal system of Vesuvius, first mineralogical and fluid inclusion data on hydrothermalized subvolcanic and lavic samples from phreatomagmatic eruptions. *Per Mineral* 64:185–187
- Fulignati P, Marianelli P, Sbrana A (1998) New insights on the thermometamorphic-metasomatic magma chamber shell of the 1944 eruption of Vesuvius. *Acta Vulcanol* 10:47–54
- Fulignati P, Marianelli P, Santacroce R, Sbrana A (2004) Probing the Vesuvius magma chamber-host rock interface through xenoliths. *Geol Mag* 141:417–428
- Fulignati P, Panichi C, Sbrana A, Caliro S, Gioncada A, Del Moro A (2005) Skarn formation at the walls of the 79AD magma chamber of Vesuvius (Italy): mineralogical and isotopic constraints. *N Jb Miner Abh* 181:53–66
- Gaeta M, Di Rocco T, Freda C (2009) Carbonate assimilation in open magmatic systems: the role of melt-bearing skarns and cumulate forming processes. *J Petrol* 50:361–385
- Ghiorso MS, Hirschmann MM, Sack RO (1994) New software models-thermodynamics of magmatic systems. *EOS Trans Am Geophys Union* 75:574–576
- Gilg HA, Lima A, Somma R, Belkin HE, De Vivo B, Ayuso RA (2001) Isotope geochemistry and fluid inclusions study of skarns from Vesuvius. *Mineral Petrol* 73:145–176
- Goff F, Love SP, Warren RG, Counce D, Obenholzner J, Siebe C, Schmidt SC (2001) Passive infrared remote sensing evidence for large, intermittent CO₂ emissions at Popocatepetl volcano, Mexico. *Chem Geol* 177:133–156
- Holloway JR (1976) Fluids in the evolution of granitic magmas: consequences of finite CO₂ solubility. *Geol Soc Am Bull* 87:1513–1518
- Holloway JR, Blank JG (1994) Application of experimental results to C–O–H species in natural melts. In: Carroll MR, Holloway JR (eds) Volatiles in magmas. *Rev Mineral* 30:187–230
- Iacono-Marziano G, Gaillard F, Pichavant M (2008) Limestone assimilation by basaltic magmas: an experimental re-assessment and application to Italian volcanoes. *Contrib Mineral Petrol* 155:719–738
- Iacono-Marziano G, Gaillard F, Scaillet B, Pichavant M, Chiodini G (2009) Role of non-mantle CO₂ in the dynamics of volcano degassing: the Mount Vesuvius example. *Geology* 37:319–322
- Iannace A, Capuano M, Galluccio L (2011) Dolomites and dolomites'' in Mesozoic platform carbonates of the Southern Apennines: geometric distribution, petrography and geochemistry. *Palaeogeogr Palaeoclimatol Palaeoecol* 310:324–339
- Iezzi G, Mollo S, Ventura G, Cavallo A, Romano C (2008) Experimental solidification of anhydrous latitic and trachytic melts at different cooling rates: the role of nucleation kinetics. *Chem Geol* 253:91–101
- Leshner CE, Hervig RL, Tinker D (1996) Self diffusion of network formers (silicon and oxygen) in naturally occurring basaltic liquid. *Geochim Cosmochim Acta* 60:405–413
- Lesne P, Scaillet B, Pichavant M, Beny J-M (2010) The carbon dioxide solubility in alkali basalts: an experimental study. *Contrib Mineral Petrol* 162:133–151
- Liang Y, Richter FM, Davis AM, Watson EB (1996) Diffusion in silicate melts I. Self diffusion in CaO–Al₂O₃–SiO₂ at 1500°C and 1 Gpa. *Geochim Cosmochim Acta* 60:4353–4367
- Metz P, Milke R (2012) Mechanism and kinetics of forsterite formation in metamorphic siliceous dolomites: finding form a rock-sample experiment. *Eur J Mineral* 24:59–72
- Mollo S, Gaeta M, Freda C, Di Rocco T, Misiti V, Scarlato P (2010) Carbonate assimilation in magmas: a reappraisal based on experimental petrology. *Lithos* 114:503–514
- Mollo S, Heap MJ, Iezzi G, Hess K-U, Scarlato P, Dingwell D (2012) Volcanic edifice weakening via decarbonation: a self-limiting processes? *Geophys Res Lett* 39:L15307. doi:10.1029/2012GL052613
- Moore G (2008) Interpreting H₂O and CO₂ contents in melt inclusions: constraints from solubility experiments and modeling. *Rev Mineral Geochem* 69:333–361
- Orsi G, De Vita S, Di Vito M (1996) The restless, resurgent Campi Flegrei nested caldera (Italy): constraints on its evolution and configuration. *J Volcanol Geotherm Res* 74:179–214
- Paone A (2006) The geochemical evolution of the Mt. Somma-Vesuvius volcano. *Mineral Petrol* 87:53–80
- Papale P, Moretti R, Barbato D (2006) The compositional dependence of the saturation surface of H₂O + CO₂ fluids in silicate melts. *Chem Geol* 229:78–95
- Peccerillo A (1999) Multiple metasomatism in central-southern Italy: geochemical effects, timing and geodynamic implications. *Geology* 27:315–318
- Peccerillo A (2005) Plio-quaternary volcanism in Italy. *Petrology, geochemistry, geodynamics*. Springer, Berlin, pp 133–135
- Perugini D, Petrelli M, Poli G (2006) Diffusive fractionation of trace elements by chaotic mixing of magmas. *Earth Planet Sci Lett* 243:669–680
- Perugini D, De Campos CP, Dingwell DB, Petrelli M, Poli G (2008) Trace element mobility during magma mixing: preliminary experimental results. *Chem Geol* 256:146–157
- Piochi M, Ayuso RA, De Vivo B, Somma R (2006) Crustal contamination and crystal entrapment during polybaric magma evolution at Mt. Somma-Vesuvius volcano, Italy: geochemical and Sr isotope evidence. *Lithos* 86:303–329
- Rittmann A (1933) Evolution and differentiation des Somma-Vesuvius-magmas. *Zs. Vulkanologie* 15:8–94
- Rolandi G, Munno R, Postiglione I (2004) The A.D. 472 eruption of the Somma volcano. *J Volcanol Geotherm Res* 129:291–319
- Schaaf P, Stimac J, Siebe C, Macias JL (2005) Geochemical evidence for mantle origin and crustal processes in volcanic rocks from Popocatepetl and surrounding monogenetic volcanoes, Central Mexico. *J Petrol* 46:1243–1282
- Somma R, Ayuso RA, De Vivo B, Rolandi G (2001) Major, trace element and isotope geochemistry (Sr–Nd–Pb) of interplinian magmas from Mt. Somma-Vesuvius (Southern Italy). *Mineral Petrol* 73:121–143

- Thirlwall MF (1991) Long-term reproducibility of multicollector Sr and Nd isotope ratio analysis. *Chem Geol* 94:85–104
- Troll VR, Hilton DR, Jolis EM, Chadwick JP, Blythe LS, Deegan FM, Schwarzkopf LM, Zimmer M (2012a) Crustal CO₂ liberation during the 2006 eruption and earthquake events at Merapi volcano, Indonesia. *Geophys Res Lett* 39:L11302. doi:10.1029/2012GL051307
- Troll VR, Deegan FM, Jolis EM, Harris C, Chadwick JP, Gertisser R, Schwarzkopf LM, Borisova AY, Bindeman IN, Sumarti S, Preece K (2012b) Magmatic differentiation processes at Merapi Volcano: inclusions petrology and oxygen isotopes. *J Volcanol Res* (in press). doi:10.16/j.jvolgeores.2012.11001
- Turi B, Taylor HP Jr (1976) Oxygen isotope studies of potassic volcanic rocks of the Roman Province, Central Italy. *Contrib Mineral Petrol* 55:1–31
- Vetere F, Botcharnikov RE, Holtz F, Behrens H, De Rosa R (2011) Solubility of H₂O and CO₂ in shoshonitic melts at 1250°C and pressures from 50 to 400 MPa: implications from Campi Flegrei magmatic systems. *J Volcanol Geotherm Res* 202:251–261
- Watson BE (1982) Basalt contamination by continental crust: some experiments and models. *Contrib Mineral Petrol* 80:73–87
- Watson EB, Jurewicz SR (1984) Behavior of alkalis diffusive of granitic xenoliths with basaltic magma. *J Geol* 92:121–131
- Watson BE, Sneeringer MA, Ross A (1982) Diffusion of dissolved carbonate in magmas: experimental results and applications. *Earth Planet Sci Lett* 61:356–358
- Werner C, Brantley S (2003) CO₂ emissions from the Yellowstone volcanic system. *Geochem Geophys Geosyst* 4(7):1061. doi:10.1029/2002GC000473
- Zhang Y (1993) A modified effective binary diffusion model. *J Geophys Res* 98:11901–11920
- Zhang Y (2010) Diffusion in minerals and melts: theoretical background. In Zhang Y, Cherniak DJ (eds) *Rev Mineral Geochem* 72:5–59
- Zhang Y, Stolper EM (1991) Water diffusion in a basaltic melt. *Nature* 351:306–309
- Zollo A, Gasparini P, Virieux J, Le Meur H, De Natale G, Biella G, Boschi E, Capuano P, De Franco R, Dell'Aversana P, De Matteis R, Guerra I, Iannaccone G, Mirabile L, Vilardo G (1996) Seismic evidence for a low-velocity zone in the upper crust beneath Mount Vesuvius. *Science* 274:592–594
- Zollo A, Gasparini P, Virieux J, Biella G, Boschi E, Capuano P, De Franco R, Dell'Aversana P, De Matteis R, De Natale G, Iannaccone G, Guerra I, Le Meur H, Mirabile L (1998) An image of Mt. Vesuvius obtained by 2D seismic tomography. *J Volcanol Geotherm Res* 82:161–173
- Zollo A, Marzocchi W, Capuano P, Lomax A, Iannaccone G (2002) Space and time behavior of seismic activity at Mt. Vesuvius volcano, Southern Italy. *Bull Seismol Soc Am* 92:625–640